

Sensing distortion-induced fatigue cracks in steel bridges with capacitive skin sensor arrays

Xiangxiong Kong ^a, Jian Li ^{a*}, William Collins ^a, Caroline Bennett ^a, Simon Laflamme ^{b,c}, and Hongki Jo ^d

^a Department of Civil, Environmental and Architectural Engineering, University of Kansas, Lawrence, KS 66045, USA

^b Department of Civil, Construction, and Environmental Engineering, Iowa State University, Ames, IA, 50011, USA

^c Department of Electrical and Computer Engineering, Iowa State University, Ames, IA, 50011, USA

^d Department of Civil Engineering and Engineering Mechanics, University of Arizona, Tucson, AZ, 85721, USA

Abstract

Distortion-induced fatigue cracks represent the majority of fatigue cracks in steel bridges in the United States. Currently, bridge owners, such as the state departments of transportation (DOTs), rely on human inspection to detect, monitor, and quantify these cracks so that appropriate repairs can be applied before cracks reach critical sizes. However, visual inspections are costly, labor intensive, and may be prone to error due to inconsistent skills among bridge inspectors. In this study, we represent a novel strain-based approach for sensing distortion-induced fatigue cracks in steel bridges using soft elastomeric capacitor (SEC) arrays. Compared with traditional foil strain gauges, the SEC technology is a large-area and flexible skin-type strain sensor that can measure a wide range of strain over a large surface. Previous investigations have verified the suitability of a single SEC for sensing an in-plane fatigue crack in a small-scale steel specimen. In this paper, we further demonstrate the ability of SECs for sensing distortion-induced fatigue cracks. The proposed strategy consists of deploying an array of SECs to cover a large fatigue-susceptible region and establishing a fatigue sensing algorithm by constructing a crack growth index (CGI) map. The effectiveness of the strategy was experimentally validated through fatigue tests of bridge girder to cross-frame connection models with distortion-induced fatigue cracks. Test results verified that by deploying an SEC array, multiple CGIs can be obtained over the fatigue-susceptible region, offering a more comprehensive picture of fatigue damage. Furthermore, by monitoring a series of CGI maps constructed under different fatigue cycles, the fatigue crack growth can be clearly visualized through the intensity change in the CGI maps.

Keywords: distortion-induced fatigue; sensing skin; structural health monitoring; capacitive strain sensor; large area electronics; steel bridges; web-gap

*Assistant Professor; Email: jianli@ku.edu

38 1. INTRODUCTION

39 Civil infrastructure systems are critical for maintaining vital societal functions. Many older bridges
40 in the United States are prone to structural damage due to carrying significant amount of service
41 loads over long periods of time. According to the recent infrastructure report [1] issued by the
42 American Society of Civil Engineers (ASCE) in early 2017, the overall score for American bridges
43 is a C+ with over 9% of the nation's bridges rated structurally deficient. These bridges require
44 significant investment in maintenance, rehabilitation, or replacement. Otherwise, structural
45 damage (e.g. cracks, corrosion, or excessive deformation) in critical structural members could
46 impair structural integrity and lead to catastrophic failures [2].

47 Among the various damage mechanisms in steel bridges, fatigue cracks are extremely common
48 [3]. In the United States, one predominate type of cracking on steel bridges is distortion-induced
49 fatigue, which is caused by out-of-plane loading in the web-gap region under differential
50 movement between adjacent girders [4]. Due to the lack of consideration in early bridge design
51 specifications, distortion-induced fatigue cracks are a common issue in many steel bridges built
52 prior to the mid-1980s in the United States [5].

53 Bridge owners, such as state departments of transportation (DOTs) in the United States, typically
54 rely on trained bridge inspectors to visually inspect steel bridges for fatigue cracking [6] so that
55 appropriate repairs can be applied before cracks reach critical sizes. However, visual inspections
56 can be prone to error due to inconsistent skills and results interpretation among inspectors [7]. For
57 instance, a study by the Federal Highway Administration (FHWA) reported that only 2 of 49 bridge
58 inspectors across the United States correctly identified fatigue cracks in steel bridges in Virginia
59 and Pennsylvania [8].

60 Advanced approaches for detecting and/or monitoring of fatigue cracks have been investigated in
61 both the structural health monitoring (SHM) and nondestructive testing (NDT) communities. As a
62 result, both the accuracy and robustness of crack detection can be improved by using sensing
63 technologies. In the context of distortion-induced fatigue crack detection, Yu et al. [9] reported an
64 acoustic emission approach for identifying fatigue damage at the fillet weld in representative
65 cruciform joints of steel bridges; Alavi et al. [10] demonstrated a self-powered sensing approach
66 based on a piezo-floating-gate (PFG) sensor for detecting distortion-induced fatigue cracks; and
67 Kong and Li [11] adopted a computer vision-based method to detect distortion-induced fatigue
68 cracks through video feature tracking. An important challenge with these methods is their reliance
69 on extensive human operations to collect critical measurements (acoustic emission data, voltage,
70 or digital videos) in the field, making it challenging to implement long-term continuous crack
71 monitoring of steel bridges.

72 Strain-based sensing methods, on the other hand, have demonstrated the ability to detect distortion-
73 induced fatigue cracks in steel bridges. By directly deploying strain sensors over crack-susceptible
74 regions, fatigue damage can be inferred by the abrupt strain change induced under cracking. For
75 instance, Ghahremani et al. [12] adopted strain gauge measurements on a large-scale bridge girder

76 to evaluate the depth characteristics of distortion-induced fatigue cracks, and Bennett et al. [13]
77 successfully used strain gages to detect the initiation of distortion-induced fatigue cracks in a test
78 of a scaled bridge. However, a general limitation of traditional metal foil strain gauges is their
79 relatively small footprint, making them less cost-effective when attempting to monitor fatigue
80 damage over a large structural surface.

81 Novel large-area strain sensing technologies, often referred to as skin sensors or sensing skins,
82 have recently attracted much attention in the SHM community, mainly attributed to their ability to
83 measure strain over a much larger area than traditional foil strain gauges. Examples include carbon
84 nanotube-based sensors [14, 15], resistive sensing sheets [16], printable conductive polymer [17],
85 patch antenna sensors [18], electrical resistance tomography [19], and so forth. These technologies
86 are all large size but rely on different sensing principles, and are used in different applications in
87 civil engineering.

88 The authors previously developed a novel skin sensor, known as soft elastomeric capacitor (SEC)
89 [20] for monitoring and detecting damage in civil structures. The SEC is a large and flexible strain
90 gauge capable of measuring up to 20% strain change over a large area [21]. SEC technology has
91 been applied in many engineering applications including: condition evaluation of wind turbine
92 blades [22], reconstruction of in-plane strain maps [23], and dynamic nondestructive testing [24].
93 The features of large sensing area and wide measurement range also make the SEC a suitable
94 candidate for crack detection and monitoring. Past research had verified the SEC's crack sensing
95 ability through numerical investigations [25] and experimental tests [26, 27, 28]. These studies
96 were mainly focused on the examination of a single SEC on a small-scale specimen with an in-
97 plane fatigue crack. However, the effectiveness of SEC technology when applied to distortion-
98 induced fatigue cracks in large-scale structures has not been investigated, and therefore remains
99 unknown.

100 In this study, we investigated the SEC's crack monitoring performance on bridge girder to cross-
101 frame connections subjected to distortion-induced fatigue. Multiple SECs were deployed over a
102 large structural region to form an SEC array. A new fatigue damage sensing approach was then
103 established in terms of crack growth index (CGI) map, which is a 2D image constructed by signals
104 from the SEC array. The CGI map offers more comprehensive fatigue-related information about
105 the monitored structural region than relying on discrete values from individual SECs. The
106 effectiveness of the SEC array and the CGI map were validated through laboratory tests on scaled
107 bridge girder to cross-frame connection models.

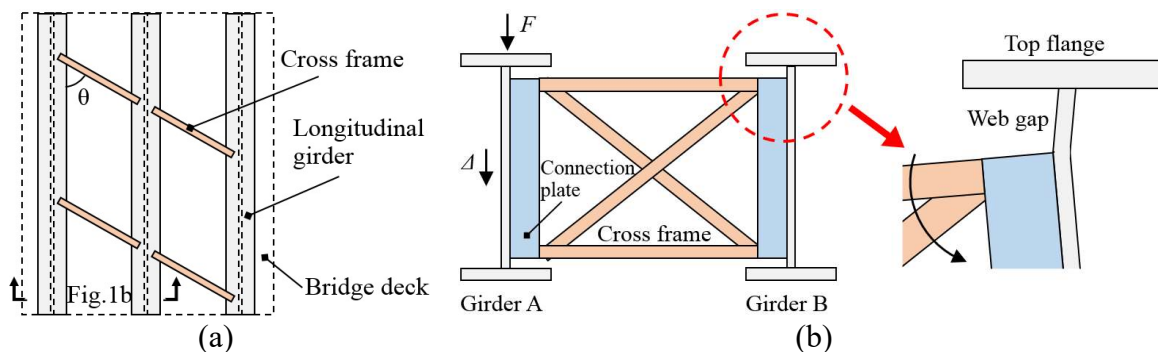
108 The rest of this paper is organized as follows: Section 2 briefly introduces the technical background
109 of distortion-induced fatigue cracks in steel bridges, the sensing principle of the SEC, and the
110 algorithm for CGI extraction; Section 3 establishes the methodology for constructing the CGI map;
111 Section 4 describes the experimental configurations; Section 5 illustrates the experimental results;
112 Section 6 further discusses the results of folded SECs from the sensor array; and Section 7
113 summarizes conclusions of the study.

114 2. BACKGROUND

115 This section introduces the background of this study including: a brief review of the mechanism
116 of distortion-induced fatigue cracking, sensing principle of the SEC, and previous work on
117 extracting fatigue sensitive features from SEC measurements.

118 2.1 Distortion-induced fatigue cracks

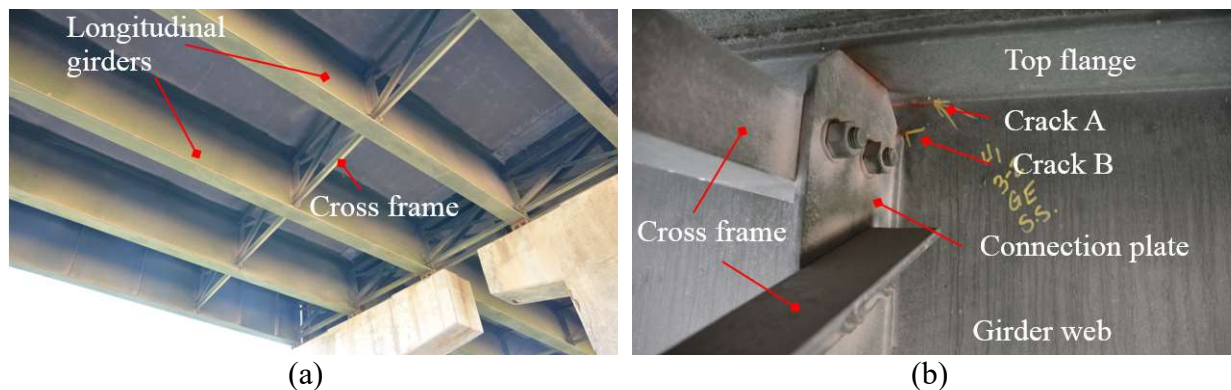
119 Figure 1 shows the mechanism of distortion-induced fatigue at web-gap regions in steel girder
120 bridges built prior to the mid-1980s in the United States. Cross-frames and diaphragms are used
121 to provide lateral stability to girders, as shown in a skewed bridge configuration in Figure 1(a). As
122 illustrated in Figure 1(b), the traffic load F applied on top of Girder A leads to a differential vertical
123 movement Δ between the two adjacent girders, which would in turn provoke an out-of-plane
124 bending moment at the top web-gap region in the adjacent girder (i.e. Girder B). This repetitive
125 out-of-plane loading leads to the initiation and propagation of fatigue cracks. A more detailed
126 discussion about the mechanism of distortion-induced fatigue cracks can be found in [29].



127 Figure 1. Schematic of a girder bridge under traffic load: (a) plan view; and (b) elevation view and
128 detail of the web-gap region.

129

130 Figure 2(a) is a photo that illustrates a common structural layout of a steel highway girder bridge.
131 Many fatigue cracks have been identified at the web-gap region in this bridge during routine bridge
132 inspections. Figure 2(b) shows a typical example where Crack A was found between the top flange
133 and web, while Crack B initiated at the top end of the fillet weld between the connection plate and
134 the web. Depending on the skew angle of the cross frame (denoted as θ in Figure 1(a)), Crack B
135 could propagate into the web region, or grow along the fillet weld between the connection plate
136 and the web.



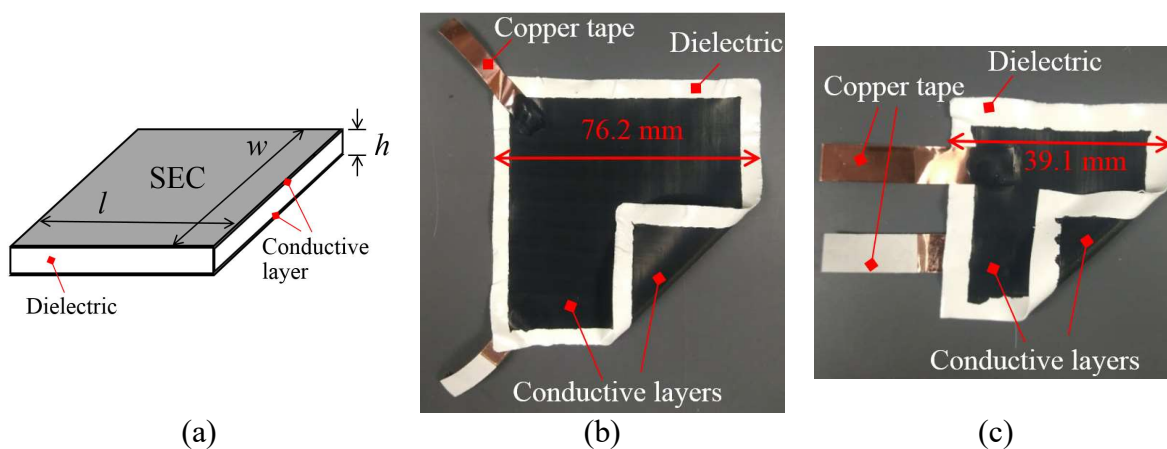
137 Figure 2. (a) A typical structural layout of a steel girder bridge in the field; and (b) representative
 138 distortion-induced fatigue cracks at the web-gap region.
 139

140 2.2 Soft Elastomeric Capacitor

141 The SEC technology is described in detail in [20]. Briefly, as shown Figure 3(a), the SEC is a
 142 large-area capacitor consisting of a dielectric layer sandwiched between two conductive layers.
 143 The two sizes of SECs adopted in this study (Figure 3(b)) are 76.2 mm by 76.2 mm (3 in. by 3 in.)
 144 and 38.1 mm by 38.1 mm (1.5 in. by 1.5 in.), with respective nominal capacitance values of
 145 approximately 900 pF and 150 pF. Two copper tapes were adhered onto both conductive layers
 146 for measuring capacitance of the sensor.

147 Equation 1 shows the sensing principle of the sensor, where C is the capacitance of the SEC, ϵ_0
 148 and ϵ_r are the vacuum and polymer relative permittivity, respectively, and l , w and h are the length,
 149 width, and thickness of the SEC (Figure 3(a)), respectively. A change in surface strain on the
 150 monitored surface will provoke a change in the geometry of the SEC (i.e. l , w , and h), hence
 151 changing the capacitance C .

152
$$C = \frac{\epsilon_0 \epsilon_r l w}{h} \quad (1)$$



153 Figure 3. (a) Schematic of the SEC; (b) photo of an SEC of dimension 76.2 mm by 76.2 mm; (c)
 154 photo of an SEC of dimension 39.1 mm by 39.1 mm.
 155

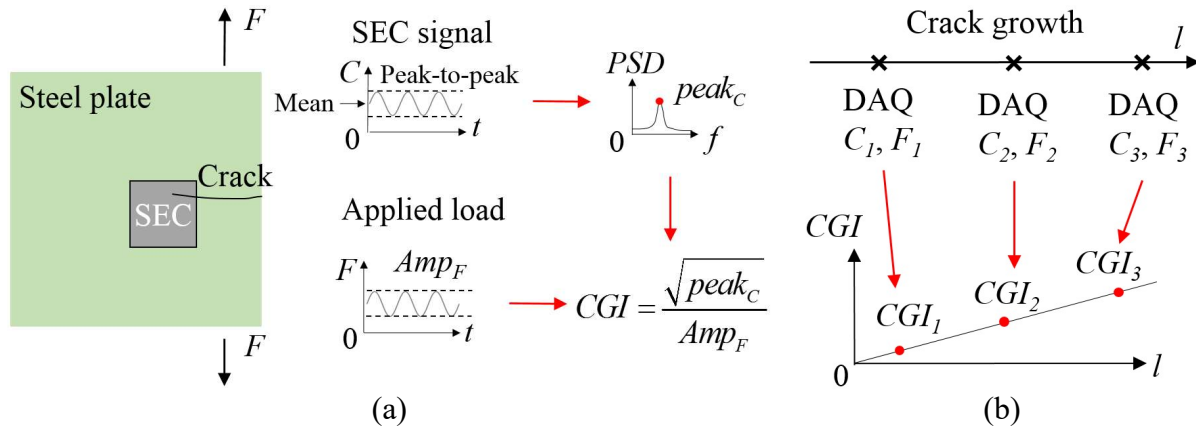
156 2.3 Crack growth index

157 Previous work [27, 30] have proposed and demonstrated a crack detection and monitoring
158 algorithm by extracting a crack-sensitive feature, termed the crack growth index (CGI), from the
159 SEC's capacitance measurements. This feature extraction method is briefly reviewed here as it
160 serves as the basis for constructing the CGI map to be introduced in Section 2.4.

161 Figure 4(a) shows the procedure for computing CGI. In the figure, a fatigue crack in a steel plate
162 is generated by the fatigue load F . An SEC is deployed onto the steel plate to monitor the crack
163 activity. Our previous investigation [27] verifies that both mean and peak-to-peak capacitances
164 (denoted in Figure 4(a)) of the SEC increase under a growing fatigue crack due to the reduction of
165 local stiffness around the crack. However, the mean capacitance is prone to drift over long-term
166 under changing environmental conditions (e.g. temperature or humidity changes). This is due to
167 an intrinsic electrical behavior found in many sensors fabricated from smart materials [31, 32].
168 The peak-to-peak capacitance, on the other side, is much less sensitive to changing environmental
169 conditions therefore serves as a robust indicator for fatigue crack growth. Directly identifying the
170 peak-to-peak capacitance from a time-series measurement is challenging because of the noise
171 content in the SEC's signal. Hence, the power spectral density (PSD) is computed to convert time-
172 series measurement into the frequency domain. The PSD curve represents the energy distribution
173 of the time-series signal, and the peak around the dominant loading frequency (denote as $peak_C$ in
174 Figure 4(a)) can robustly indicate the peak-to-peak capacitance.

175 The magnitude of the applied load F is also required for CGI extraction. This is because the load
176 range (denote as Amp_F in Figure 4(a)) also directly affects the peak-to-peak capacitance of the
177 SEC. A larger load range would induce higher capacitance response even if the crack does not
178 grow. Hence, the capacitance response needs to be normalized with respect to the load range,
179 which leads to the equation $CGI = \sqrt{peak_C} / Amp_F$. The applied fatigue load can either be directly
180 measured from the actuator in a laboratory setting or indirectly inferred via strain measurements
181 in practical applications.

182 Once the CGI is extracted from one set of short measurements, crack growth can be monitored
183 through a long-term monitoring strategy as illustrated in Figure 4b. Briefly, a series of short-time
184 measurements of the applied load F and capacitance response C are collected during the fatigue
185 life of the steel plate. If the crack grows between the data collection intervals, the extracted CGI
186 would increase. By collecting the CGIs through repeated measurements over time, the fatigue
187 crack growth can be monitored. It should be noted that the absolute value of CGI is also governed
188 by the type of normalizer. The normalization procedure for computing CGIs could be based on the
189 applied load from the actuator in the laboratory or the strain measurement from the strain gauge
190 installed in the steel bridge. Therefore, directly comparing CGIs from different test set-ups or
191 normalizers is not meaningful. However, for a predetermined test set-up with a fixed normalizer,
192 the relative change of CGIs (i.e. the increasing trend in Figure 4b) is a robust indicator of fatigue
193 crack growth.



194 Figure 4. (a) Methodology for extracting CGI from a single dataset; and (b) correlating CGI with
 195 crack lengths based on multiple datasets. DAQ in Figure 4b represents data acquisition.

196 3. METHODOLOGY

197 Previous research has focused on the examination of a single SEC on a small-scale specimen with
 198 an in-plane fatigue crack. The method of CGI extraction reviewed in Section 2.3 was developed
 199 for single SEC utilization. However, for sensing distortion-induced fatigue cracks in steel bridges,
 200 an array of SECs is adopted in this study to cover a larger fatigue-susceptible region. As the number
 201 of SECs increases in this application, measurements from the SEC array result in multiple CGIs.
 202 Investigating the CGI change for each individual SEC against different crack lengths would be
 203 time-consuming and less informative. A better approach is to spatially visualize all CGIs of the
 204 SEC array over the fatigue-susceptible region. We do so by extending the CGI index to a CGI map
 205 to visually represent the spatial distribution of CGIs.

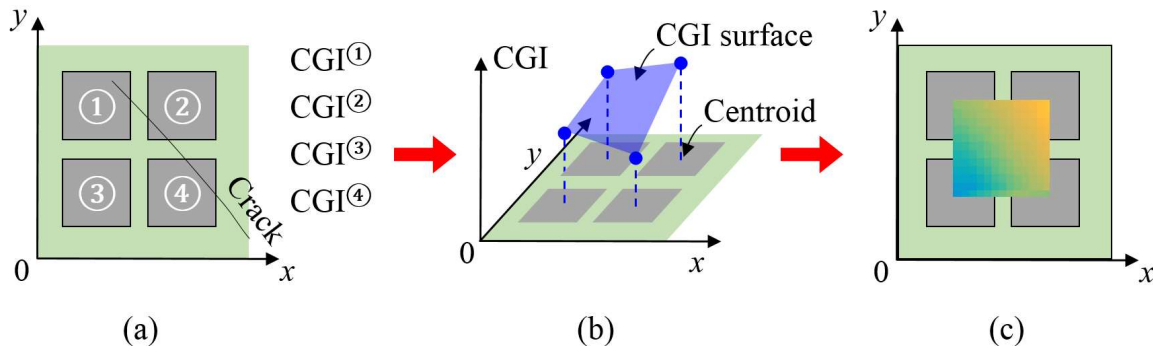
206 3.1 CGI map

207 Figure 5 illustrates the methodology for constructing a CGI map. An array of SECs was deployed
 208 on a steel plate to monitor the crack growth, and $CGI^{(1)}$, $CGI^{(2)}$, $CGI^{(3)}$, and $CGI^{(4)}$ are the CGI
 209 values for each individual SEC (Figure 5(a)). Where a crack propagates under an SEC (e.g. $SEC^{(1)}$,
 210 $SEC^{(2)}$, and $SEC^{(4)}$ in Figure 5(a)), the CGI is a direct indicator of crack growth. On the other hand,
 211 where the crack does not grow under an SEC (e.g. $SEC^{(3)}$ in Figure 5a), the SEC serves as a large-
 212 area strain gauge for monitoring migration of the strain field caused by the crack growth.

213 Next, the CGIs of the four SECs in Figure 5(a) were mapped to a 3D coordinate system where the
 214 vertical axis is the magnitude of CGI and the two horizontal axes represent the plane of the
 215 structural surface. The CGIs are placed at the centroid of each SEC as shown in Figure 5(b).
 216 Subsequently, a 3D CGI surface was created using linear interpolation. The 3D CGI surface is a
 217 matrix that contains the interpolated CGIs over the zone defined by the four centroids of the SEC
 218 array. Finally, by projecting the CGI surface to the structural surface, the 2D image, termed the
 219 CGI map, can be constructed as illustrated in Figure 5c.

220 By constructing a series of CGI maps based on multiple measurements from the SEC array at
 221 different crack lengths, fatigue damage in a large region can be monitored. If the fatigue crack

222 does not grow during the data collection intervals, the corresponding CGI maps would exhibit a
223 similar intensity distribution. Conversely, fatigue crack propagation would provoke intensity
224 changes in the CGI maps, which serve as good features for fatigue damage monitoring.



225 Figure 5. (a) Methodology for constructing CGI map: (a) individual CGIs from an SEC array; (b)
226 a CGI surface through linear interpolation; and (c) CGI map. The SECs in Figure 5(a) is illustrated
227 as transparent for illustration purpose.
228

229 3.2 Special considerations for distortion-induced fatigue cracks

230 Section 3.1 presented the methodology for constructing CGI maps through a steel plate under an
231 in-plane fatigue crack. However, distortion-induced fatigue cracks in steel bridges usually initiate
232 and propagate along complex paths, as they are subjected to multi-directional states of stress that
233 can vary significantly within the web-gap region. As illustrated in Figure 2(b), distortion-induced
234 fatigue cracks may initiate between the girder web and top flange (e.g. Crack A), or between the
235 connection plate and girder web (e.g. Crack B). In both cases, cracking initiates at the weld toe
236 between two adjacent structural components. Furthermore, depending on the structural geometric
237 layout, the crack may continue to grow along the weld. Hence, special considerations are needed
238 for detecting distortion-induced fatigue cracks.

239 Previous studies [27, 28] validated that the SEC can effectively sense in-plane fatigue damage if
240 the crack directly propagates under the sensing skin. However, to detect a distortion-induced
241 fatigue crack that grows along the weld, the SEC may need to be deployed in a folded configuration.
242 For instance, an SEC should be folded to cover both the connection plate and the girder web to
243 detect Crack B shown in Figure 2(b).

244 4. EXPERIMENTAL CONFIGURATION

245 4.1 Description of the test set-up

246 A bridge girder to cross-frame connection was adopted for the experimental tests in this study, as
247 shown in Figure 6. To simulate the restraint provided to the top flange of a bridge girder by the
248 deck in the field, the bridge girder was mounted upside-down to the strong floor in the laboratory
249 to constrain the bottom flange of the girder. A cross frame was then installed to the girder through
250 a connection plate. The skew angle θ between the cross frame and the girder was 40 degrees as
251 shown in Figure 6(b). To represent the structural layout of typical girder bridges built prior to the

1980s, the connection plate (Figure 6(c)) was only fillet welded to the girder web while the top and bottom of the connection plate were not attached to the flanges. A detailed description of the test specimen can be found in Yu et al. [33].

It should be noticed that the girder to cross-frame connection in this study is a simplified subassembly of the entire bridge system without considering the effect of bridge deck. In addition, the bending behavior of the steel girder due to dead and live loads are eliminated, while only out-of-plane bending imposed by the movement of cross-frame is obtained. Nevertheless, Hassel et al. [34] performed a comparative study through more than 1,000 large-scale finite element (FE) simulations. The study concluded that the stress fields at the web-gap region of the subassembly FE models were similar to the ones extracted from the global bridge FE models. Similar type of subassembly was adopted in the experimental studies in [35] as well.

To apply fatigue load cycles, an actuator was vertically attached to the far end of the cross frame. The actuator was restrained from moving laterally (Figure 6(a)) so that it could only move in the vertical direction and apply vertical load to the cross frame. A 0.5 Hz harmonic load was adopted and a load range of -4.9 kN (-1.1 kip) to 4.9 kN (1.1 kip) was applied.

The dominant frequency of the traffic load cycles in the field depends on multiple factors such as the speed of the passing vehicle, the span length of the steel girder, and girder boundary conditions. The 0.5 Hz frequency adopted in this study is within the range of field measurements performed by McElrath [36]. The load range of fatigue cycles, on the other side, was determined by considering the stress range at the web-gap region, vertical displacement of the cross frame, and crack growth rate. Yu et al. [33] applied a fatigue cycle of 0 kN (0 kip) to 10.2 kN (2.3 kip) to the same test model and demonstrated the rationale for such a load range design. In this study, we adopted the similar load range (2.2 kip) under a symmetric distribution (± 1.1 kip) in order to consider the reversal behavior of the traffic load in the field.

As mentioned in Section 2.3, the amplitude of the applied load is required for extracting the CGI from the SEC's capacitance measurement. For this purpose, a strain gauge was installed on the top horizontal cross frame member (Figure 6(b)) to indirectly infer the amplitude of applied load during the test. A similar strategy could be applied in field applications where the true fatigue load caused by passing vehicles cannot be easily measured.

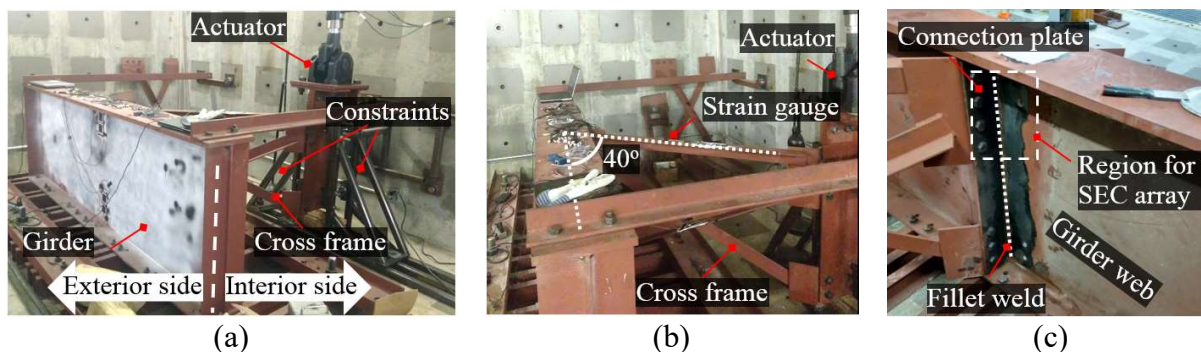


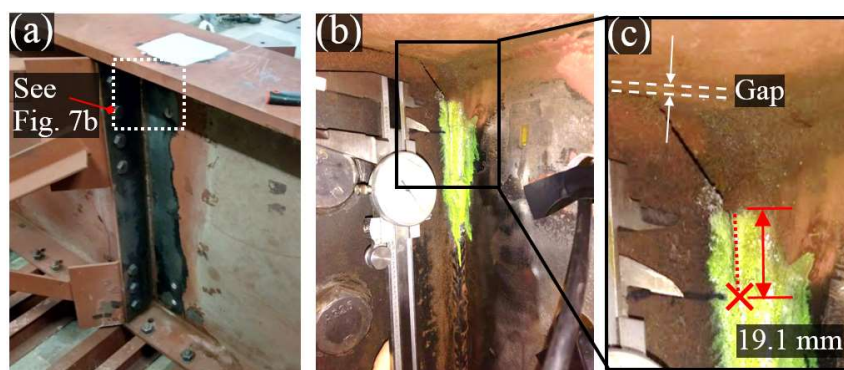
Figure 6. (a) Exterior view of the test model; (b) interior view of the test model; and (c) detailed view of the connection plate. Figure 6(c) shows the specimen prior to installation of the SEC array.

283

284 4.2 Existing fatigue damage

285 Prior to this study, the test model had been fatigue loaded for 2.7 million cycles under a load range
286 of 0 to 11.2 kN (2.5 kip). As a result, a fatigue crack existed at the interior side of the top web-gap
287 region between the connection plate and the girder web. Due to the small opening of the fatigue
288 crack, a fluorescent dye penetrant was used to accurately identify the locations of the crack tip. As
289 shown in Figure 7, the length of the fatigue crack was measured as 19.1 mm (0.75 in.).

290 Figure 7(c) shows the detailed layout at the top web gap region of the connection model. The
291 connection plate was not welded to the girder flange, leaving a gap between the flange and
292 connection plate, which was the primary reason for causing distortion-induced fatigue cracks as
293 discussed in Section 2.1.



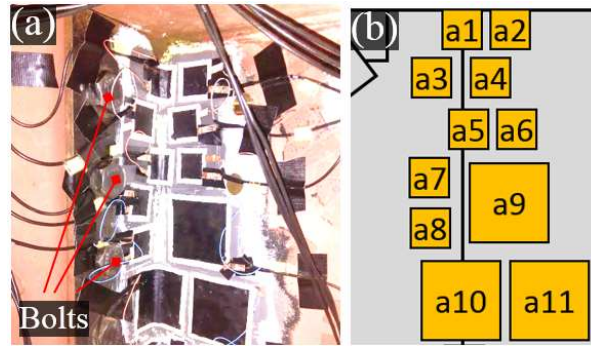
294 Figure 7. Existing fatigue damage in the connection model: (a) overview; (b) fatigue crack at the
295 top region of the connection; and (c) detailed look of Figure 7(b).

296

297 4.3 Deployment of an SEC array

298 To detect and monitor distortion-induced fatigue damage in the test girder, an SEC array was
299 deployed at the top web-gap region, as shown in Figure 8(a). SECs with dimensions 76.2 mm x
300 76.2 mm (3 in. x 3 in.) are termed large SECs, while those with dimensions 38.1 mm x 38.1 mm
301 (1.5 in. x 1.5 in.) are termed small SECs. A total of 11 SECs were deployed on the structural
302 surface using a bi-component epoxy (JB Weld). Figure 8(b) schematizes the sensor layout. Folded
303 SECs (i.e. SEC a1, a5, and a10) were deployed along the weld to detect crack growth at the weld
304 toes. Flat SECs, on the other hand, were intended to serve as large-area strain gauges to sense the
305 strain field migration caused by cracking activity. Small SECs a3, a7, and a8 were deployed at the
306 connection plate in order to avoid the conflict of existing structural bolts (denoted in Figure 8(a)).
307 Our previous studies [25] validated that small SECs were more sensitive to fatigue crack growth
308 by producing higher percentage of capacitance changes. Therefore, in this experimental program,
309 small SEC a1 to a6 were deployed at the top region of the SEC array with aim to better quantifying
310 the crack activities. An off-the-shelf data acquisition (DAQ) system (ACAM PCAP02) was used
311 to collect the capacitance measurements of the SEC array.

312 The number of SECs in a SEC array for monitoring a fatigue crack in practice varies depending
313 on multiple factors such as: the location of the crack, the layout of the bridge, existing length of
314 the crack, and the crack growth rate estimated by engineering knowledge. For example, a single
315 SEC can be enough for monitoring a short, slow-propagating crack; while multiple SECs are
316 required in order to sense a lengthy, fast-growing fatigue crack, which is the situation in this
317 experimental program. A more detailed discussion can be found in [28].

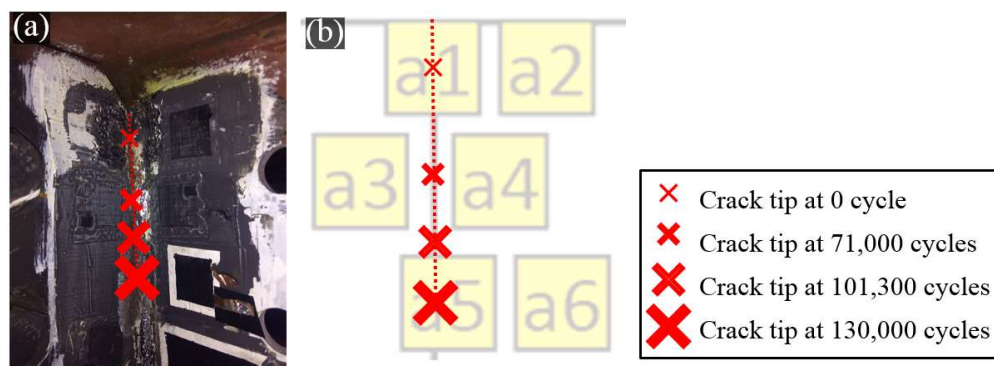


318 Figure 8. (a) SEC array arrangement; and (b) a schematic of the sensor layout.
319

320 4.4 Experimental procedure

321 During the test, 130,000 new load cycles were applied to the test girder under the load range of -
322 4.9 kN (-1.1 kip) to +4.9 kN (+1.1 kip). A total of 13 datasets were collected at cycle counts of 0,
323 15,000, 21,500, 30,000, 43,100, 53,800, 64,900, 79,200, 93,000, 101,300, 110,000, 121,000, and
324 130,000. Each dataset contained both capacitance measurements from the SEC array and the strain
325 gauge collected over 2-min periods, sampled at 50 Hz and 2000 Hz, respectively. During the test,
326 four inspections were performed to identify crack lengths at cycle counts of 0, 71,000, 101,300,
327 and 130,000 cycles, respectively.

328 Figure 9(a) presents a photograph of the specimen at the end of the test, in which some of the SECs
329 were removed to clearly identify the crack tip. The locations of the crack tips identified from the
330 four inspections are marked in Figure 9(a) and (b). The length of the crack was measured from the
331 top end of the weld, as annotated in Figure 9(a). Crack lengths were approximately 19 mm (0.8
332 in.), 42 mm (1.7 in.), 62 mm (2.5 in.), and 84 mm (3.3 in.), respectively at the time of the four
333 inspections. This result indicates how the fatigue crack propagated over the 13 data collection
334 intervals.



335 Figure 9. (a) Locations of the crack tips at different cycle counts; and (b) illustration of crack tips
336 with respect to the sensor layout.
337

338 SEC a1 was removed after 79,200 load cycles, shown in Figure 10. The bonded side (i.e. the side
339 in direct contact with the steel surface) of SEC a1 experienced damage during loading. In particular,
340 a crack was identified in the conductive layer of SEC a1, exposing a white line that revealed the
341 dielectric layer. This crack in the SEC was attributed to the large out-of-plane crack opening
342 displacement under the sensor that repeatedly stretched the sensing skin during the test. Despite
343 the occurrence of the crack in the conductive layer, SEC a1 continued providing capacitance data
344 as to be illustrated in Figure 13.

345



346 Figure 10. (a) SEC a1 was removed after 79,200 load cycles for a detailed inspection. On the
347 bonded side (the side in direct contact with the steel surface) of the SEC, a crack was identified in
348 the conductive layer, indicating damage to the SEC. The white color along the crack is the exposed
349 dielectric layer.

350 5. EXPERIMENTAL RESULTS

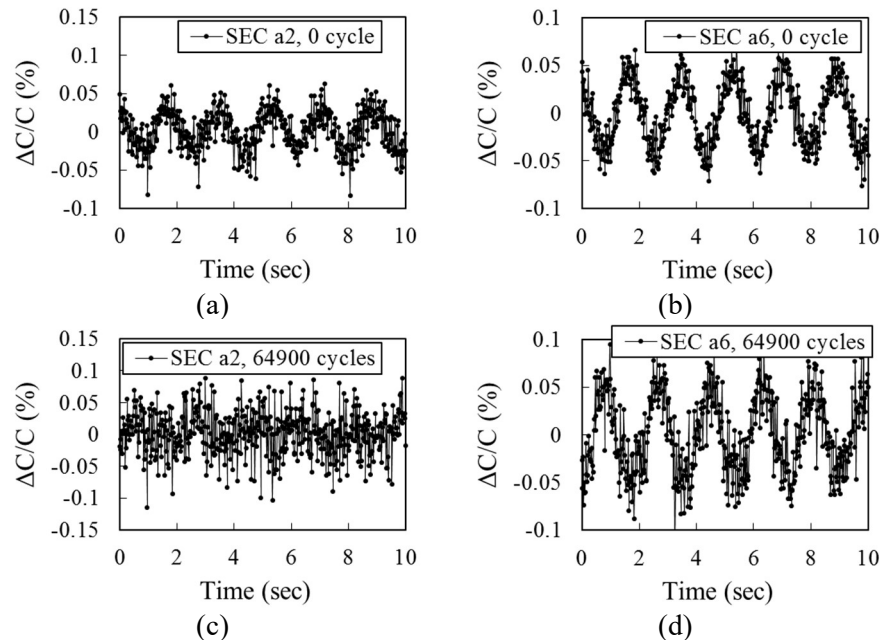
351 5.1 Representative time-series measurements

352 Figure 11 presents a series of plots of representative time-series measurements of the SEC array
353 taken from SECs a2 and a6. The plots present 10 seconds of measurements collected at 0 cycles
354 (the beginning of the test) and 64,900 cycles. SEC a2 initially exhibited a larger peak-to-peak
355 capacitance $\Delta C/C$ (Figure 11(a)), which became significantly smaller after 64,900 cycles (Figure
356 11(c)). This reduction may be attributed to the crack tip propagating away from SEC a2, causing

357 strain relief around SEC a2 (Figure 9(b)). SEC a6, which was located in front of the crack
358 propagation path, experienced an increased peak-to-peak capacitance, $\Delta C/C$, at 64900 cycles due
359 to higher strain caused by the crack tip moving closer to the sensor.

360 As discussed in Section 2.3, although peak-to-peak capacitance is a good indicator of fatigue crack
361 growth, it is often times difficult to reliably identify in time-series signals due to the noise content.
362 This can be observed in the signals plotted in Figure 11. Therefore, CGIs were extracted from the
363 time-series signals through frequency analysis described in the next subsection.

364



365 Figure 11. Representative time-series measurements from the SEC array. (a) SEC a2 at 0 cycle;
366 (b) SEC a6 at 0 cycle; (c) SEC a2 at 64,900 cycles; and (d) SEC a6 at 64,900 cycles.

367

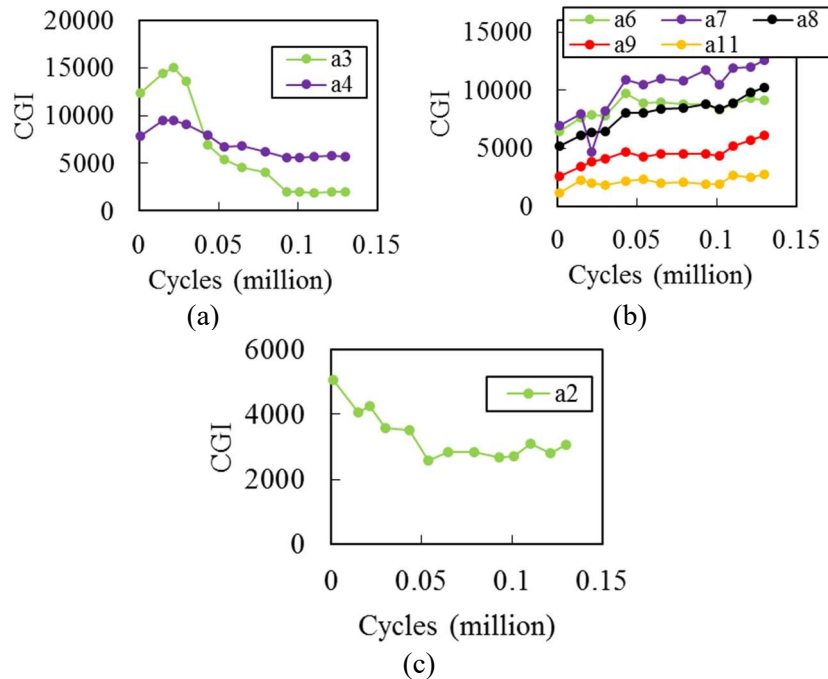
368 5.2 CGIs from the SEC array

369 5.2.1 CGIs from the flat SECs

370 CGIs were extracted from the SEC array using the method introduced in Section 2.3. The strain
371 measurement at the top chord of the cross frame was used to normalize the SEC measurements.
372 Figure 12 shows the CGIs from the flat SECs at different numbers of load cycles. For clarity,
373 results have been grouped based on the similarity of amplitude of CGI response.

374 As shown in Figure 12(a), CGIs from SEC a3 and a4 quickly increased at the beginning of the test
375 and then gradually decreased. This phenomenon was a result of crack propagation which initially
376 brought the crack tip closer to a3 and a4 during the first three datasets collected (0, 15,000, and
377 21,500 cycles). The stress concentration around the crack tip increased the responses of nearby
378 sensors. As the crack propagated further and the crack tip moved beyond a3 and a4, the stress relief

379 along the fatigue crack path led to a decrease in the responses of these two sensors after 21,500
380 cycles.



381 Figure 12. CGIs for (a) SEC a3 and a4; (b) SEC a6, a7, a8, a9, and a11; and (c) SEC a2.
382

383 Figure 12(b) shows the CGIs from SECs a6, a7, a8, a9, and a11, in which increasing CGIs were
384 observed for all SECs. This increasing trend was due to increases in the strain field at these SECs
385 caused by crack growth. SEC a7 experiences a drop at 21,500 cycles. This is probably due to the
386 noisy content of this particular measurement, leading to a lower energy magnitude at 0.5 Hz in the
387 PSD curve. Figure 12(c) illustrates the CGI change for SEC a2. As the crack propagated downward,
388 stress relief along the crack path led to a decreasing trend of CGI as shown in the figure. This
389 behavior is corroborated by comparing time-series measurements shown in Figure 11(a) and (c),
390 in which the peak-to-peak capacitance decreased significantly at 64,900 cycles.

391 5.2.2 CGIs from the folded SECs

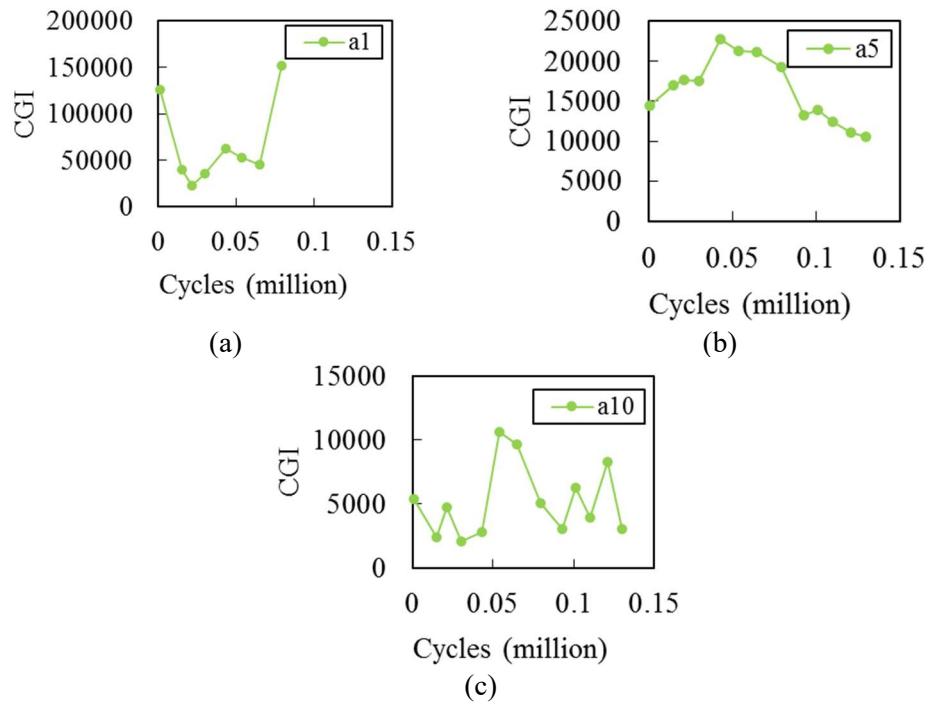
392 SECs a1, a5, and a10 were folded at the corner between the connection plate and the girder web.
393 CGIs from these three SECs have been plotted in Figure 13. Only eight datasets were collected for
394 SEC a1, after which the sensor was removed for a detailed inspection (see discussion in Section
395 4.4). SEC a1 exhibited significantly higher CGI responses than the other SECs. In addition, the
396 CGIs from SEC a1 exhibited fluctuations during the test. This behavior is caused by the damage
397 occurring in the sensing material of SEC a1 (Figure 10) provoked by the distortion-induced fatigue
398 cracking.

399 SEC a5 also exhibited much larger CGI responses than adjacent flat SECs. The initial CGI from
400 SEC a5 was approximately 14,400 while the CGIs from SEC a6 and a7 were approximately 6,500
401 and 7,000, as shown in Figure 12(b). This is due to the relative rotation between the connection

402 plate and the girder web, which periodically stretches the sensing skin around the corner,
403 provoking additional capacitance change to the SEC. In addition, the CGIs from SEC a5 (Figure
404 12b) steadily increased at the beginning of the test, and then decreased after 43,100 cycles.
405 However, based on the observation illustrated in Figure 9(b), the fatigue crack reached SEC a5 at
406 approximately 100,000 cycles and propagated to the center of SEC a5 at 130,000 cycles (end of
407 the test). The CGI from SEC a5 continuously decreased during this stage despite the fact that the
408 fatigue crack was growing under the sensing skin. A detailed discussion about the possible cause
409 of this phenomenon can be found in Section 6.

410 Figure 13(c) shows the CGI from SEC a10, which is a folded sensor located far away from the
411 fatigue crack. Large fluctuations were observed in the CGIs collected throughout the test from this
412 SEC. The fluctuations may be attributed to the fact that SEC a10 was far away from the fatigue
413 crack, and hence was less sensitive to the fatigue crack growth.

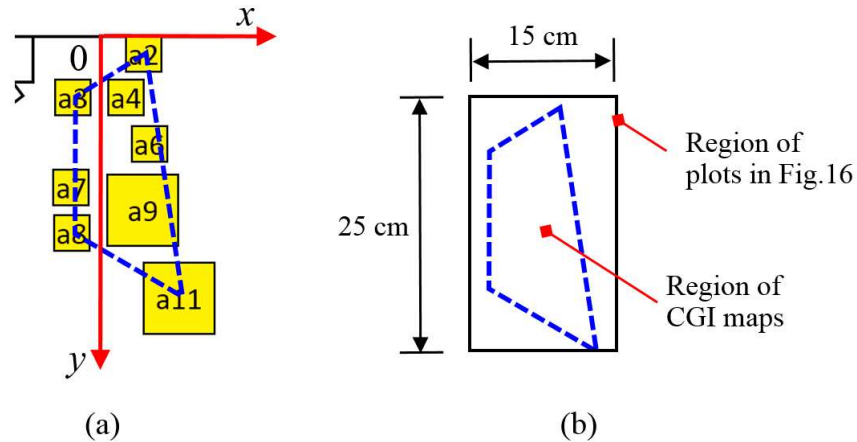
414 In summary, CGIs from folded SECs, initially deployed for directly detecting the crack growth,
415 were unable to fulfil such a purpose (i.e. fluctuations of CGIs in SEC a1 and a10; decreasing CGIs
416 when the crack grew into SEC a5). In this regard, only the flat SECs were adopted for constructing
417 CGI maps, presented in the next subsection.



418 Figure 13. CGIs from (a) SEC a1; (b) SEC a5; (c) SEC a10

419 5.3 CGI maps

420 CGI maps were constructed using CGIs from the SEC array. Figure 14(a) illustrates the flat SECs
421 used in constructing the CGI maps. The dashed lines represent the boundaries of the CGI maps. A
422 2D coordinate system was created where the origin was at the top of the weld. Figure 14(b)
423 schematizes the 15 cm x 25 cm (6 in. x 10 in.) region used as the boundary for the plots shown in
424 Figure 15.



(a)

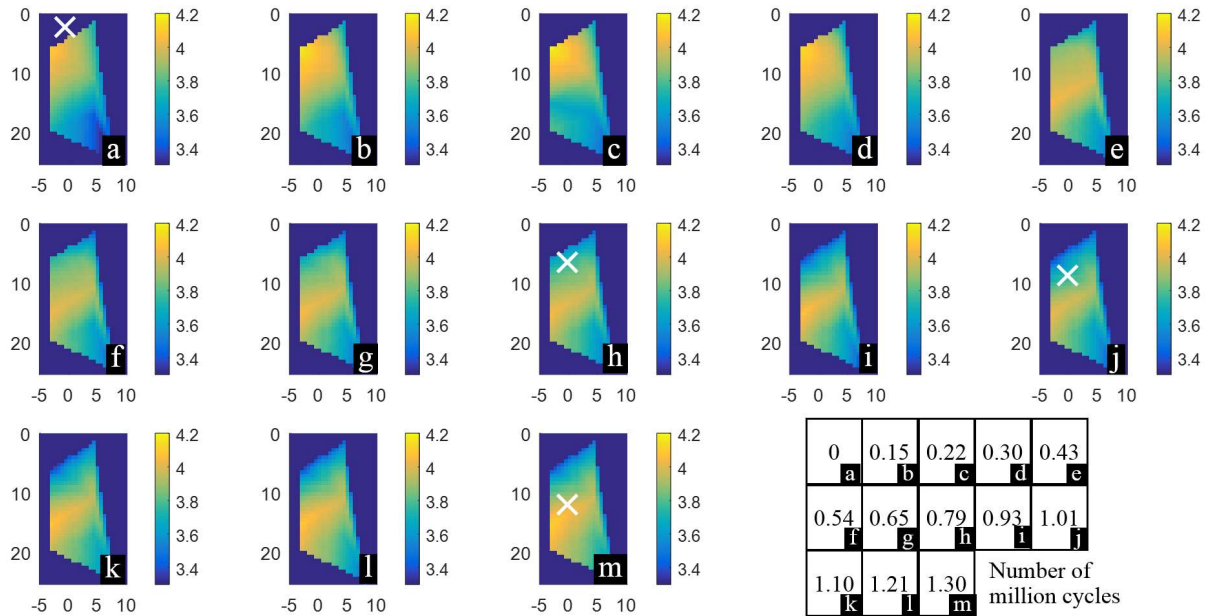
(b)

Figure 14. SECs for constructing the CGI maps.

425
426

427 Figure 15 shows the resulting CGI maps. Due to significant differences in magnitudes of CGIs
428 (e.g. the CGI was as large as 15,000 for SEC a3, and approximately 2,000 for SEC a11), the
429 intensity in the CGI maps is represented in logarithmic scale. The CGI map covers a large area of
430 fatigue susceptible region (10 cm by 20 cm). The crack tip locations were identified multiple times
431 during the test, which are also marked with white x's in Figure 15a, h, j and m.

432 Each plot in Figure 15 illustrates the distribution of CGI for the SEC array corresponding to each
433 data collection interval, enabling a clear depiction of the fatigue damage over this large area. As
434 the number of load cycles increases, the intensity in the CGI map changes. For instance, as the
435 crack tip moved downward (shown in the progressions of Figure 15 (a) to (d)), higher
436 intensities/brightness can be observed in the top-left region of the CGI map. However, as the crack
437 continued to propagate, the top-left region became darker due to the stress relief along the crack
438 path, as demonstrated in the progression shown in Figure 15e to h. The bottom-left corner of the
439 CGI map became brighter during crack propagation, evident in a comparison of Figure 15h and m.
440 This is due to the increasing strain field provoked by the propagation of the crack. By comparing
441 the CGI map between the beginning and the end of the test (i.e. Figure 15 (a) and (m)), significant
442 changes in the location of high CGI intensity can be observed, indicating the fatigue crack
443 propagation behavior during these 13 data collection intervals.

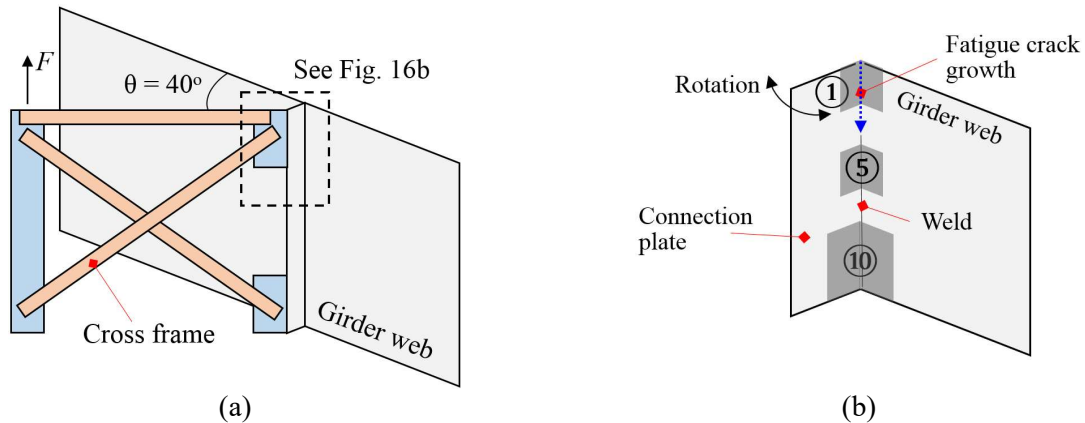


444 Figure 15. CGI maps at the top region of the connection under different load cycles. The 'x' at a,
 445 h, j and m indicate the locations of the crack tips observed during the test. The number of load
 446 cycles associated with each plot is shown at the bottom-right corner of this figure.
 447

448 6. FURTHER DISCUSSION ON FOLDED SEC SENSORS

449 This section investigates the potential source of the electromechanical behavior of the folded SEC
 450 a5 described in Section 5.2.2. SEC a5 was initially deployed for directly detecting the crack growth,
 451 but did not yield increasing CGIs when the crack propagated through the sensor. Figure 16
 452 schematizes the layout of the test model, in which there is a skew angle of 40 degrees between the
 453 cross frame and the girder web. Due to the skewed configuration, the fatigue load F creates both a
 454 vertical movement of the cross frame and a horizontal rotation around the girder web, as illustrated
 455 in Figure 16b. Such a rotational movement could lead to a supplemental change in capacitance of
 456 the SEC folded between the connection plate and girder web. As a result, the folded SEC a5 is
 457 subject to a combined effect of crack propagation and cross frame rotation, which may have
 458 contributed to the behavior of SEC a5.

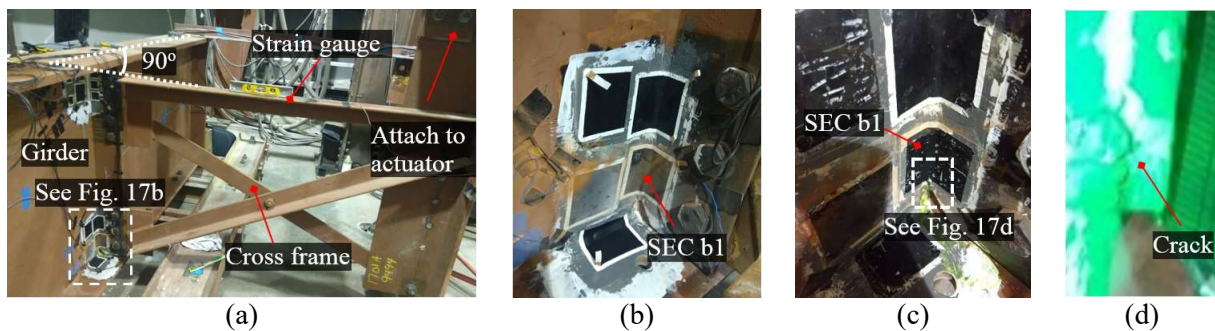
459



460 Figure 16. (a) An illustration of the rotation between the connection plate and the girder web in
 461 the tested model; and (b) inset detail at the top web gap (other SECs not shown for clarity).

462

463 To further validate this hypothesis, an additional experimental investigation was performed on a
 464 non-skewed bridge girder to cross frame connection model, as shown in Figure 17(a). This new
 465 model is similar to the skewed one described in section 4.1, except that the cross frame is
 466 perpendicular to the girder web, as denoted in Figure 17(a). The test model was symmetric about
 467 the cross frame. This non-skewed structural layout allowed the cross frame to maintain the vertical
 468 movement under the fatigue loading without being subject to the horizontal rotation around the
 469 girder web.



470 Figure 17. (a) Test set-up of the non-skewed bridge girder to cross frame connection; (b) SEC b1
 471 at the bottom region of the connection (other SECs are note related with this study); (c) SEC b1
 472 was removed for crack inspection after the fatigue test; and (d) crack inspection result.

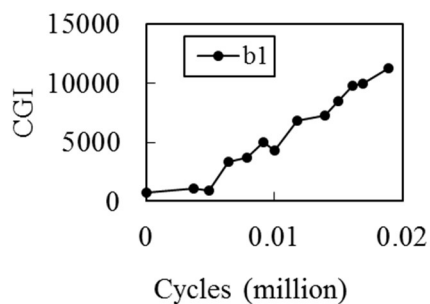
473

474 An SEC, denoted SEC b1 in Figure 17(b), was deployed in folded configuration along the weld
 475 between the connection plate and the girder web. A foil strain gauge was installed on the top chord
 476 of the cross frame for normalizing the SEC's measurement. Prior to the test, the test model was
 477 inspected and no fatigue crack was detected. The test model was then fatigue loaded with 18,900
 478 cycles with a load range of 2.2 kN to 25.5 kN (0.5 kip to 5.75 kip), leading to a newly-initiated
 479 fatigue crack beneath SEC b1. After the test, SEC b1 was removed to confirm the crack activity

480 (Figure 17(c)). The fatigue crack is shown in Figure 17(d) under fluorescent dye penetrant.
481 Compared with previous skewed test model in Section 4, higher load range is adopted here in order
482 to generate a similar level of stress at the web-gap region. Even though the load ranges are different
483 in these two experimental configurations, the CGI extraction demonstrated in Section 2.3 is based
484 on the normalized peak-to-peak capacitance of the SEC, hence is insensitive with magnitudes of
485 load ranges.

486 During the test, 13 short time measurements of both the SEC and the strain gauge were collected
487 for computing the CGIs. Utilizing the same CGI extraction method, CGIs of SEC b1 were
488 computed and plotted in Figure 18. A clearly increasing trend of CGIs is observed in the figure,
489 indicating SEC b1 was able to successfully monitor the crack growth, despite its folded
490 configuration.

491 A comparison between the two tests with folded SECs under the skewed and non-skewed bridge
492 configurations reveals that the rotational movement occurring between the girder web and
493 connection plate led to the inability of the folded SEC a5 to provide consistently increasing CGIs
494 under crack propagation. When no such rotational movement is occurring, as it is the case for the
495 non-skewed configuration, the folded SEC b1 was able to provide robust CGIs to monitor crack
496 growth. Therefore, folded configuration of the SECs is only recommended to use in non-skewed
497 bridge configurations or in ones with small skewness that have limited rotations.



498
499 Figure 18. CGIs from SEC b1 in the non-skewed bridge girder to cross frame connection

500 7. CONCLUSIONS

501 This study presented a novel strain-based approach for sensing out-of-plane distortion-induced
502 fatigue cracks in steel bridges using soft elastomeric capacitor (SEC) arrays. The SEC is a large-
503 area and flexible sensing skin, able to measure a wide range of strains over large structural surfaces.
504 Previous investigations have verified the ability of a single SEC for sensing an in-plane fatigue
505 crack in a small-scale specimen. In this study, we further demonstrated the ability of the SEC
506 technology in the context of sensing distortion-induced fatigue cracks, which represent the
507 majority of fatigue cracks in aging steel highway girder bridges in the United States.

508 With the proposed strategy, multiple SECs in the form of a sensor array were deployed to cover a
509 large fatigue-susceptible region. Subsequently, a fatigue sensing algorithm was proposed by

510 constructing a crack growth index (CGI) map from the measurements of the SEC array. The
511 effectiveness of the SEC array coupled with the CGI map was then experimentally validated
512 through a fatigue test of a bridge girder to cross-frame connection model subjected to distortion-
513 induced fatigue. Test results verified that by deploying the SEC array, multiple CGIs can be
514 obtained over the fatigue-susceptible region, offering a comprehensive picture of the fatigue
515 damage. Furthermore, through monitoring the evolution of CGI maps constructed under different
516 fatigue load cycles, the fatigue crack growth can be clearly visualized by identifying the intensity
517 changes in the CGI maps.

518 Comparison between the skewed and non-skewed bridge configurations also indicated that the
519 horizontal rotation between the connection plate and the girder web can affect the effectiveness of
520 the folded SEC for directly monitoring crack growth along the corner of the connection. This
521 observation provides an important guideline for applying the SECs in folded configuration in
522 future field applications. A more cost-effective sensor deployment approach in this case would be
523 to attach flat SECs along both sides of the crack path such that the crack growth can be monitored
524 through the migration of the strain field caused by the crack activity. Alternatively, performing
525 fundamental experimental studies regarding the behavior of the folded SEC under rotational
526 movement would also be helpful to address this challenges.

527 **ACKNOWLEDGEMENT**

528 This work was supported by the Transportation Pooled Fund Study, TPF-5(328), which includes
529 the following participating state Departments of Transportation (DOTs): Kansas, Iowa, Minnesota,
530 North Carolina, Pennsylvania, Texas, and Oklahoma; and Iowa Department of Transportation
531 grant #RT454-494. Their support is gratefully acknowledged. The authors also want to thank
532 undergraduate research assistant Sam Tankel from the University of Kansas for helping with the
533 skewed bridge girder test, PhD students Danqing Yu from the University of Kansas for creating
534 the test set-up of the skewed bridge girder test and assisting with the test operation, PhD student
535 Hayder Al-Salih from the University of Kansas for helping with the non-skewed bridge girder test,
536 PhD student Austin Downey from the Iowa State University for providing support regarding the
537 data acquisition system, and Justin Ocel from the Federal Highway Administration (FHWA) for
538 providing valuable feedback to the test program.

539 **REFERENCES**

- [1] American Society of Civil Engineers (ASCE). (2017). 2017 Infrastructure Report Card –
Bridges, <https://www.infrastructurereportcard.org/wp-content/uploads/2017/01/Bridges-Final.pdf>
- [2] Biezma, M. V., & Schanack, F. (2007). Collapse of steel bridges. *Journal of Performance of
Constructed Facilities*, **21**(5), 398-405.
- [3] Fisher, J. W. (1984). *Fatigue and fracture in steel bridges. Case studies*.

- [4] Connor, R. J., & Fisher, J. W. (2006). Identifying effective and ineffective retrofits for distortion fatigue cracking in steel bridges using field instrumentation. *Journal of Bridge Engineering*, **11**(6), 745-752.
- [5] Zhao, Y., & Roddis, W. M. K. (2004). Fatigue Prone Steel Bridge Details: Investigation and Recommended Repairs, *K-TRAN: KU-99-2, Final Report*. Kansas Department of Transportation, Topeka, KS.
- [6] Federal Highway Administration (FHWA). (2004). *National bridge inspection standards*, Federal Register, 69 (239).
- [7] Zhao Z, and Haldar A. (1996). Bridge fatigue damage evaluation and updating using non-destructive inspections. *Engineering fracture mechanics*. **53**(5), 775-88.
- [8] Holusha, J. and Chang, K. (2007). Engineers see dangers in aging infrastructure. New York Times, August 2, 2007. <http://www.nytimes.com/2007/08/02/us/01cnd-engineer.html>
- [9] Yu, J., Ziehl, P., Matta, F., & Pollock, A. (2013). Acoustic emission detection of fatigue damage in cruciform welded joints. *Journal of Constructional Steel Research*, **86**, 85-91.
- [10] Alavi, A. H., Hasni, H., Jiao, P., Borchani, W., & Lajnef, N. (2017). Fatigue cracking detection in steel bridge girders through a self-powered sensing concept. *Journal of Constructional Steel Research*, **128**, 19-38.
- [11] Kong, X. and Li, J. (2018). Vision-based fatigue crack detection of steel structures using video feature tracking. *Computer-Aided Civil and Infrastructure Engineering*. In press.
- [12] Ghahremani, K., Sadhu, A., Walbridge, S., & Narasimhan, S. (2013). Fatigue testing and structural health monitoring of retrofitted web stiffeners on steel highway bridges. Transportation Research Record: *Journal of the Transportation Research Board*, (2360), 27-35.
- [13] Bennett, C., Matamoros, A., Barrett-Gonzalez, R., & Rolfe, S. (2014). Enhancement of Welded Steel Bridge Girders Susceptible to Distortion-Induced Fatigue. *Final Report for Transportation Pooled-Fund Study TPF-5(189)*, June, 2014.
- [14] Dai H, Thostenson ET, and Schumacher T. (2015). Processing and Characterization of a Novel Distributed Strain Sensor Using Carbon Nanotube-Based Nonwoven Composites. *Sensors*. **15**(7), 17728-47
- [15] Ahmed, S., Thostenson, E. T., Schumacher, T., Doshi, S. M., & McConnell, J. R. (2018). Integration of carbon nanotube sensing skins and carbon fiber composites for monitoring and structural repair of fatigue cracked metal structures. *Composite Structures*.
- [16] Yao Y, and Glisic B. (2015). Detection of steel fatigue cracks with strain sensing sheets based on large area electronics. *Sensors*. **15**(4), 8088-108
- [17] Loh KJ, Kim J, Lynch JP, Kam NW, and Kotov NA. (2007). Multifunctional layer-by-layer carbon nanotube-polyelectrolyte thin films for strain and corrosion sensing *Smart Materials and Structures*. **16**(2), 429.
- [18] Yi X, Cho C, Cooper J, Wang Y, Tentzeris MM, and Leon RT. (2013). Passive wireless antenna sensor for strain and crack sensing - electromagnetic modeling, simulation, and testing. *Smart Materials and Structures*. **22**(8), 085009

- [19] Smyl, D., Pour-Ghaz, M., & Seppänen, A. (2018). Detection and reconstruction of complex structural cracking patterns with electrical imaging. *NDT & E International*.
- [20] Laflamme S, Kollosche M, Connor JJ, and Kofod G. (2012). Robust flexible capacitive surface sensor for structural health monitoring applications *Journal of Engineering Mechanics*. **139** 879-85.
- [21] Laflamme S, Saleem HS, Vasani BK, Geiger RL, Chen D, Kessler MR, and Rajan K. (2013). Soft elastomeric capacitor network for strain sensing over large surfaces. *IEEE/ASME Transactions on Mechatronics*. **18** 1647-54.
- [22] Downey, A., Laflamme, S., & Ubertini, F. (2017). Experimental wind tunnel study of a smart sensing skin for condition evaluation of a wind turbine blade. *Smart Materials and Structures*, **26**(12), 125005.
- [23] Downey, A., Laflamme, S., & Ubertini, F. (2016). Reconstruction of in-plane strain maps using hybrid dense sensor network composed of sensing skin. *Measurement Science and Technology*, **27**(12), 124016.
- [24] Saleem, H., Downey, A., Laflamme, S., Kollosche, M., & Ubertini, F. (2015). Investigation of dynamic properties of a novel capacitive-based sensing skin for nondestructive testing. *Materials Evaluation*, **73**(10), 1384-1391.
- [25] Kong, X., Li, J., Bennett, C., Collins, W., & Laflamme, S. (2016). Numerical simulation and experimental validation of a large-area capacitive strain sensor for fatigue crack monitoring. *Measurement Science and Technology*, **27**(12), 124009.
- [26] Kharroub S, Laflamme S, Song C, Qiao D, Phares B, and Li J. (2015). Smart sensing skin for detection and localization of fatigue cracks. *Smart Materials and Structures*. **24** 065004.
- [27] Kong, X., Li, J., Collins, W., Bennett, C., Laflamme, S., & Jo, H. (2017). A large-area strain sensing technology for monitoring fatigue cracks in steel bridges. *Smart Materials and Structures*, **26**(8), 085024.
- [28] Kong, X., Li, J., Collins, W., Bennett, C., Laflamme, S., & Jo, H. (2018). Thin-Film Sensor for Fatigue Crack Monitoring in Steel Bridges Under Varying Crack Growth Rate and Random Traffic Load. *ASCE Journal of Aerospace Engineering*, Accepted.
- [29] Jajich, D., & Schultz, A. E. (2003). Measurement and analysis of distortion-induced fatigue in multigirder steel bridges. *Journal of Bridge Engineering*, **8**(2), 84-91.
- [30] Kong, X., Li, J., Collins, W., Bennett, C., Laflamme, S., & Jo, H. (2017, April). A robust signal processing method for quantitative high-cycle fatigue crack monitoring using soft elastomeric capacitor sensors. In *Sensors and Smart Structures Technologies for Civil, Mechanical, and Aerospace Systems 2017 (Vol. 10168, p. 101680B)*. International Society for Optics and Photonics.
- [31] Cai L, Song L, Luan P, Zhang Q, Zhang N, Gao Q and Zhou W 2013 Super-stretchable, transparent carbon nanotube-based capacitive strain sensors for human motion detection *Sci. Rep.* **3** 3048
- [32] Kang I, Schulz M J, Kim J H, Shanov V and Shi D 2006 A carbon nanotube strain sensor for structural health monitoring *Smart Mater. Struct.* **15** 737

- [33] Yu, D., Bennett, C., & Matamoros, A. Retrofitting Distortion-Induced Fatigue in Skewed Girders to Cross-Frame Connections. *In Structures Congress 2017* (pp. 149-161).
- [34] Hassel, H. L., Bennett, C. R., Matamoros, A. B., & Rolfe, S. T. (2012). Parametric analysis of cross-frame layout on distortion-induced fatigue in skewed steel bridges. *Journal of Bridge Engineering*, 18(7), 601-611.
- [35] Alemdar, F., Nagati, D., Matamoros, A., Bennett, C., & Rolfe, S. (2013). Repairing distortion-induced fatigue cracks in steel bridge girders using angles-with-plate retrofit technique. I: Physical simulations. *Journal of Structural Engineering*, 140(5), 04014003.
- [36] McElrath, K. S. (2015). Field, Laboratory, and Analytical Investigation of Angles-with-Plate Retrofit for Distortion-Induced Fatigue in Steel Bridges (Doctoral dissertation, University of Kansas).